



CHORUS

This is the accepted manuscript made available via CHORUS. The article has been published as:

Quantum Variational Learning of the Entanglement Hamiltonian

Christian Kokail, Bhuvanesh Sundar, Torsten V. Zache, Andreas Elben, Benoît Vermersch, Marcello Dalmonte, Rick van Bijnen, and Peter Zoller

Phys. Rev. Lett. **127**, 170501 — Published 22 October 2021

DOI: [10.1103/PhysRevLett.127.170501](https://doi.org/10.1103/PhysRevLett.127.170501)

Quantum Variational Learning of the Entanglement Hamiltonian

Christian Kokail^{*},^{1,2} Bhuvanesh Sundar^{*},^{1,3} Torsten V. Zache,^{1,2} Andreas Elben,^{1,2,4}
Benoît Vermersch,^{2,1,5} Marcello Dalmonte,^{6,7} Rick van Bijnen,^{1,2} and Peter Zoller^{1,2}

¹*Institute for Quantum Optics and Quantum Information of the Austrian Academy of Sciences, Innsbruck A-6020, Austria*

²*Center for Quantum Physics, University of Innsbruck, Innsbruck A-6020, Austria*

³*JILA, Department of Physics, University of Colorado, Boulder CO 80309, USA^{*}*

⁴*Institute for Quantum Information and Matter and Walter Burke Institute for Theoretical Physics, California Institute of Technology, Pasadena, CA 91125, USA*

⁵*Univ. Grenoble Alpes, CNRS, LPMMC, 38000 Grenoble, France*

⁶*The Abdus Salam International Center for Theoretical Physics, Strada Costiera 11, 34151 Trieste, Italy*

⁷*SISSA, via Bonomea 265, 34136 Trieste, Italy*

Learning the structure of the entanglement Hamiltonian (EH) is central to characterizing quantum many-body states in analog quantum simulation. We describe a protocol where spatial deformations of the many-body Hamiltonian, physically realized on the quantum device, serve as an efficient variational ansatz for a local EH. Optimal variational parameters are determined in a feedback loop, involving quench dynamics with the deformed Hamiltonian as a quantum processing step, and classical optimization. We simulate the protocol for the ground state of Fermi-Hubbard models in quasi-1D geometries, finding excellent agreement of the EH with Bisognano-Wichmann predictions. Subsequent on-device spectroscopy enables a direct measurement of the entanglement spectrum, which we illustrate for a Fermi Hubbard model in a topological phase.

Introduction – Significant progress has been made in developing quantum simulation hardware [1, 2]. In atomic physics, analog quantum simulators for Bose and Fermi Hubbard models are realized with ultracold atoms in optical lattices [3–10], and spin models can be implemented with Rydberg tweezer arrays [11–13] and trapped ions [14, 15]. A notable recent development is spatial and temporal control, allowing addressing of single lattice sites, and single-shot single-site read out of atoms [1, 2], e.g. as spin and density resolved measurements with a quantum gas microscope [16, 17]. The generic many-body Hamiltonian realized in analog quantum simulators has a (quasi-) local structure, $\hat{H}(\mathbf{g}) = \sum_i g_i \hat{h}_i$, where the \hat{h}_i act non-trivially on spatially contiguous sites i as few-body operators. Achieving local control thus implies tunability of the spatial couplings g_i . Analog quantum simulators are, therefore, capable of not only realizing homogeneous, i.e. ‘in-bulk’ translationally invariant Hamiltonians $\hat{H} = \sum_i \hat{h}_i$, but a whole family of spatially *deformed Hamiltonians* $\hat{H}(\mathbf{g})$ with a spatiotemporally programmable pattern $\mathbf{g} \equiv \{g_i\}$. This programmability provides us with opportunities to design specific classes of quantum protocols, running on the quantum simulator, to achieve tasks of interest in quantum many-body physics.

Below we describe a protocol based on a hybrid classical-quantum algorithm [18] to learn the entanglement Hamiltonian (EH) of a subsystem A of a quantum many-body state [see Eq. 1]. In the protocol, a *deformed Hamiltonian* $\hat{H}_A^{\text{var}}(\mathbf{g})$ plays the role of an *ansatz for the EH*, where \mathbf{g} represents a small set of variational parameters scaling polynomially with the system size. These are determined efficiently in a quantum feedback loop from monitoring the time evolution of certain local, experi-

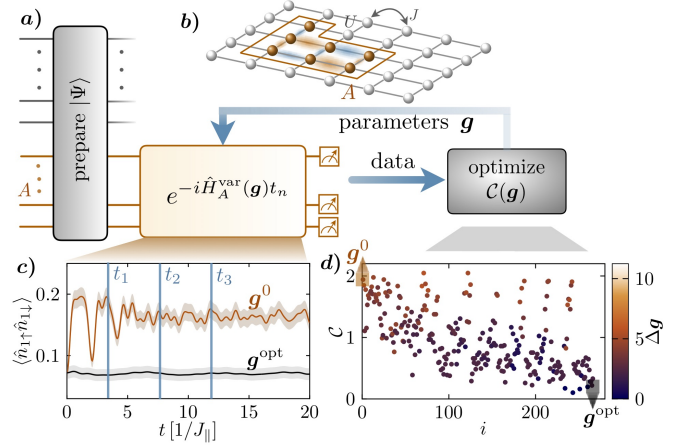


FIG. 1. *Quantum variational learning (QVL) of EH* a) subsystem A is time-evolved with the deformed Hamiltonian $\hat{H}_A^{\text{var}}(\mathbf{g})$, while measuring observables $\langle \hat{O}_A \rangle_t$ at time instances $\{t_n\}$. A classical computer optimizes a cost function $C(\mathbf{g})$ in a feedback loop, minimizing the time variation of observables. b) Fermi Hubbard Model, and subsystem A . c) Time variation of observables indicating convergence in the feedback loop from the initial \mathbf{g}^0 to final \mathbf{g}^{opt} parameters, d) corresponding cost function vs. iteration number of the optimizer. The colormap visualizes the distance to the final parameter vector $\Delta \mathbf{g} = |\mathbf{g}^i - \mathbf{g}^{\text{opt}}|$. Data plotted in c) and d) were obtained in simulated runs for a 2-leg Fermi-Hubbard ladder [see text and Fig. 2a),b)], monitoring double site occupancy by means of a quantum gas microscope.

mentally accessible observables evolving under $\hat{H}_A^{\text{var}}(\mathbf{g})$. As outlined in Fig. 1a), our protocol differs from classical learning (CL) methods [19–22] by implementing a quantum processing step through time evolution with the deformed Hamiltonian, acting *in situ* on the quantum

state stored in quantum memory of the quantum simulator. A unique feature of the present setting is that the learned EH is also available as a physical Hamiltonian on the quantum device for further experimental studies, such as, e.g., determining the entanglement spectrum (ES) through spectroscopy. This is in contrast to tomography-based methods [23, 24], where the ES is obtained by diagonalizing the (learned) EH on a classical computer.

We emphasize that by devising variational quantum algorithms in the framework of analog simulation we build on existing, scalable and high-fidelity quantum hardware, capable of realizing physically motivated variational ansätze for the EH. As illustrated below, this hardware efficiency includes the ability to represent fermions in Hubbard models naturally as fermionic atoms and associated fermionic quantum operations. While digital algorithms [25–31] offer in principle a broader scope of applicability, they come in general with the significant hardware requirement of a freely programmable quantum computer and involve a technical overhead for realising fermionic models.

Ansatz for EH as deformed Hamiltonian – The entanglement Hamiltonian (EH) \tilde{H}_A and the collection of its eigenvalues $\{\xi_\alpha\}$, the entanglement spectrum (ES), are central to our understanding of complex quantum states as they completely characterize all correlations in a subsystem A . Given a many-body state $\hat{\rho}$, they are related to the reduced density matrix on A via

$$\hat{\rho}_A \equiv \text{Tr}_{-A}[\hat{\rho}] \equiv \exp(-\tilde{H}_A) = \sum_{\alpha} e^{-\xi_{\alpha}} |\Phi_A^{\alpha}\rangle \langle \Phi_A^{\alpha}|. \quad (1)$$

The ES can distinguish different quantum phases, e.g. its low-lying part reflects the structure of the conformal field theory (CFT) describing edge excitations in a topological phase [32, 33]. Moreover, the EH plays a key role in the holographic approach to geometry emerging from entanglement [34].

In many physically relevant cases, \tilde{H}_A is a *deformation* of the system Hamiltonian \hat{H} . A seminal example is provided by the Bisognano-Wichmann (BW) theorem of local quantum field theory (QFT) [35]. It states that the EH for the ground state of a relativistic QFT and a subsystem A defined by $x_1 > 0$ is given by $\tilde{H}_A = \int_{\mathbf{x} \in A} d\mathbf{x} \beta(\mathbf{x}) \hat{\mathcal{H}}(\mathbf{x}) + c$. Here $\hat{\mathcal{H}}(\mathbf{x})$ is the energy density of \hat{H} , c is a normalization constant and the EH is parametrized by a local “inverse temperature” $\beta(\mathbf{x}) = 2\pi x_1$, taking the form of a linear ramp. We emphasize that the BW theorem holds in arbitrary spatial dimensions [36]. Remarkably, BW-like deformations also provide excellent approximations for the EH of the ground state in a variety of lattice models [37–40]. Based on this observation, Ref. [41] proposed that, *assuming* the validity of a lattice version of the BW theorem, the BW-deformed Hamiltonian can be physically realized and probed in quantum simulation experiments. In contrast,

our hybrid classical-quantum learning algorithm explicitly *finds* the optimal variational approximation for the EH among a class of deformed system Hamiltonians.

Protocol – The key ingredient of the algorithm is the capability of the quantum simulator to realize unitary evolution under deformed Hamiltonians $\hat{H}_A^{\text{var}}(\mathbf{g}) = \sum_{j \in A} g_j \hat{h}_j$, acting for some time t on a subsystem of interest A . As illustrated in Fig. 1a, we first prepare a desired quantum state, then evolve the subsystem according to $\hat{H}_A^{\text{var}}(\mathbf{g})$, and monitor the evolution of local observables \hat{O}_A in the subsystem,

$$\langle \hat{O}_A \rangle_t \equiv \text{Tr}_A \left[\hat{O}_A e^{-i\hat{H}_A^{\text{var}}(\mathbf{g})t} \hat{\rho}_A e^{i\hat{H}_A^{\text{var}}(\mathbf{g})t} \right]. \quad (2)$$

The classical-quantum feedback loop consists in finding an optimal set \mathbf{g}^{opt} by minimizing the time variation of the observables, i.e. we wish to enforce $\langle \hat{O}_A \rangle_t = \text{const}$. In practice, we achieve this by minimizing a cost function $\mathcal{C}(\mathbf{g}) = \sum_{t \in T, \hat{O}_A \in O} \left(\langle \hat{O}_A \rangle_t - \langle \hat{O}_A \rangle_0 \right)^2$, where $T = \{t_i\}$ denotes a set of observation times. The precise choice of observables \hat{O}_A is not critical for our protocol, as we expect the quantum dynamics to scramble them into complex many-body operators as long as $[\hat{O}_A, \hat{H}_A^{\text{var}}(\mathbf{g})] \neq 0$.

Thus, monitoring a small number of local observables at different observation times $\{t_i\}$ provides a sufficient number of constraints for the algorithm to find an optimal variational approximation to the EH. This is efficient in view of the quasi-local ansatz with a small set of variational parameters, and we refer to the Supplemental Material [42] for a detailed technical discussion, including the choice of observables and the role of conservation laws.

We note that the EH is obtained from Eq. (2) only up to a scale factor and an overall shift, $\tilde{H}_A^{\text{var}} = \beta \hat{H}(\mathbf{g}^{\text{opt}}) + c$, i.e. the ES is determined as universal ratios, $\kappa_{\alpha} = (\xi_{\alpha} - \xi_{\alpha_0}) / (\xi_{\alpha_1} - \xi_{\alpha_0})$. As discussed in the Supplemental Material [42], which includes the references [43–47], these scale factors can be determined in additional steps.

Learning the EH of ground states of the Fermi-Hubbard model – We now demonstrate the quantum EH learning protocol for the Fermi-Hubbard model (FHM). The FHM is a paradigmatic model in condensed matter physics for a strongly interacting quantum many-body system, and in two spatial dimensions (2D) is central to studies of high-temperature superconductivity. The FHM is described by the Hamiltonian

$$\begin{aligned} \hat{H}_{\text{FHM}} = & -J \sum_{\langle jk \rangle, \sigma} \left(\hat{c}_{j\sigma}^{\dagger} \hat{c}_{k\sigma} + \text{H.c.} \right) \\ & + U \sum_j \hat{n}_{j\uparrow} \hat{n}_{j\downarrow} - \mu \sum_{j\sigma} \hat{n}_{j\sigma}, \end{aligned} \quad (3)$$

with $\hat{c}_{j\sigma}$ ($\hat{c}_{j\sigma}^{\dagger}$) destruction (creation) operators for fermions on lattice site j with spin $\sigma = \{\uparrow, \downarrow\}$. The

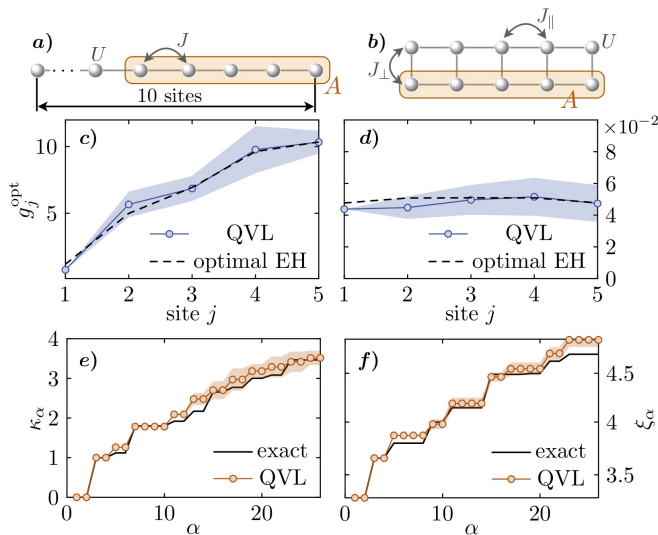


FIG. 2. *Quantum variational learning (QVL) of the EH for different geometries of a Hubbard model.* Left column: results for a 5-site subsystem on the right boundary of a 10-site Hubbard chain with $U/J = 1$ and $\mu/J = -0.5$. Right column: results for a single chain in a 2-leg ladder with $U/J_{\parallel} = 8$, $J_{\perp}/J_{\parallel} = 2$ and $\mu/J = 0$. a), b) lattice geometries with highlighted subsystems. c), d) variational parameters g_j^{opt} obtained from optimization with 6×10^4 experimental runs (QVL), fixing $g_{j=1}$. The optimal parameters are rescaled (corresponding fidelities shown in Fig. 3) for comparison with the EH parameters obtained by numerically optimizing the relative entropy (black solid lines, see also Supplemental Material [42]). e), f) Universal ratios κ_{α} calculated by diagonalizing the variationally obtained EH $\hat{H}_A^{\text{var}}(\mathbf{g}^{\text{opt}})$ in comparison to exact eigenvalues of the reduced density matrix ρ_A . All simulations are performed for the ground state in the zero magnetization sector. Error bands are computed by repeating the entire optimization run 10 times and computing the standard error.

first term describes hopping of particles with tunneling strength J between neighboring sites $\langle jk \rangle$, the second term represents an on-site interaction with strength U with densities $\hat{n}_{j\sigma} = \hat{c}_{j\sigma}^{\dagger} \hat{c}_{j\sigma}$, and the last term involves chemical potentials μ_{σ} . The FHM is realized in state-of-the-art quantum simulators employing fermionic atoms trapped in optical lattices [5–8].

We illustrate quantum variational learning (QVL) of the EH structure for the FHM with two examples (see Fig. 2). The first example considers a 1D chain with subsystem A on the right boundary [Fig. 2a)]. The second example is a two-leg ladder, which is cut horizontally defining A as the lower leg [Fig. 2b)]. For the two-leg ladder, we consider a slight modification to the FHM with anisotropic hopping $J \rightarrow J_{\parallel}, J_{\perp}$ between horizontal and vertical links, respectively. In both FHM examples, we assume the total system is in its ground state with half filling, and in the zero magnetization sector. As an ansatz for the deformed Hamiltonian to be learned for these examples, we choose $\hat{H}^{\text{var}}(\mathbf{g}) = \sum_{j \in A} g_j \hat{h}_j$, defined on a

subsystem A , with quasi-local operators centered on lattice site j :

$$\hat{h}_j = - \sum_{k \in \langle jk \rangle \cap A} \sum_{\sigma} \frac{J}{2} (\hat{c}_{j\sigma}^{\dagger} \hat{c}_{k\sigma} + \text{H.c.}) + U \hat{n}_{j\uparrow} \hat{n}_{j\downarrow} - \mu \sum_{\sigma} \hat{n}_{j\sigma}, \quad (4)$$

where for the horizontally cut ladder, $J = J_{\parallel}$. We note that for the full system, $\hat{H}_{\text{FHM}} \equiv \sum_j \hat{h}_j$, and that the ansatz $\hat{H}^{\text{var}}(\mathbf{g}) = \sum_{j \in A} g_j \hat{h}_j$ can thus be viewed as a discretized lattice version of the BW deformation, as originally defined in the continuum. Realizing such a deformed Hamiltonian in the laboratory requires local control over the Hamiltonian parameters J, U , and μ_{σ} , which can be achieved e.g. by using digital mirror devices to shape optical potentials [48], and through Raman induced laser couplings [49]. Alternatively, time evolution with a deformed Hamiltonian can also be naturally implemented as digital quantum simulation, achieved with spatially homogeneous Hamiltonians acting for short times on properly chosen subregions of A (see Supplemental Material [42]).

We numerically simulate the full protocol of determining the EH (Fig. 1), including quantum projective measurements and variational optimization with an adaptive DIRECT algorithm, as used in Ref. [15], constraining the total number of experimental runs to 6×10^4 . As observables to be monitored, we choose the double occupancy on lattice sites for the first example [50], and for the second example local tunneling elements $\mathcal{J}_{j,j+1}^{\sigma} = \hat{c}_{j\sigma}^{\dagger} \hat{c}_{j+1,\sigma} + \text{H.c.}$, which can be accessed by inducing superexchange oscillations accompanied by site-resolved measurements in a quantum gas microscope [51, 52].

For the 1D Hubbard chain, Fig. 2c) shows the optimized parameters \mathbf{g}^{opt} , consistent with the BW expectation of an approximately linear ramp, but bending over to a parabolic shape due to boundary effects. For the two-leg FHM with horizontal cut, Fig. 2 d) shows the learned deformation as approximately flat, again in agreement with a minimal version of BW. We can understand this result perturbatively in the limit $U \gg J_{\perp/\parallel}$ for $J_{\perp} \gg J_{\parallel}$. In this case, following [53], the EH is proportional to the system Hamiltonian restricted to a single leg of the ladder.

Having learned the operator structure of the EH $\hat{H}^{\text{var}}(\mathbf{g}^{\text{opt}}) = \sum_j g_j^{\text{opt}} \hat{h}_j$, and having a realization of the EH available as physical Hamiltonian on the quantum device, we can proceed to extract entanglement properties encoded in the EH with both classical or quantum (on device) postprocessing. Below we focus on the entanglement spectrum, which is obtained either by diagonalizing the EH classically, or via ‘on device’ spectroscopy, which potentially scales to regimes beyond classical postprocessing.

Classical postprocessing of the EH – Fig. 2e,f) shows universal ratios κ_{α} obtained by diagonalizing the learned

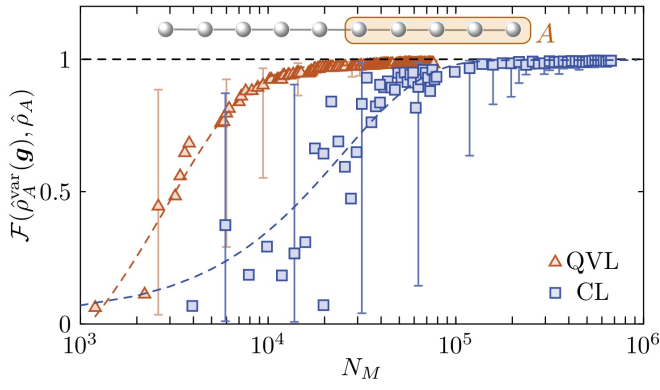


FIG. 3. *Error assessment vs. number of experimental runs* N_M : Maximally achievable Uhlmann fidelity with respect to the exact density matrix $\hat{\rho}_A$ as a function of the total number of measurements for a half-partition of a 10-site Hubbard chain ($N_A = 5$) for $U/J = 1$ as shown in the inset. For comparison, the blue data points represent a learning protocol based on classical post-processing of measurement data [19]. The data show the median of the fidelity when the experiment is repeated 100 times. We plot a selection of representative error bars which indicate 2σ confidence intervals.

EH. The results compare favorably to the exact values within 2σ error bands. To further quantify the performance of the EH reconstruction, we compare in Fig. 3b) the Uhlmann fidelity $\mathcal{F}(\hat{\rho}_A^{\text{var}}(\mathbf{g}), \hat{\rho}_A)$ [54] of the reconstructed state $\hat{\rho}_A^{\text{var}}(\mathbf{g})$ with respect to the exact density matrix $\hat{\rho}_A$ as a function of the total number of experimental runs. The analysis is performed for a 5-site subsystem on the right boundary of a 10-site Hubbard chain as depicted in Fig. 3. We present results for a parametrization of the form $\hat{H}_A^{\text{var}}(\mathbf{g}) = \sum_{j \in A} g_j \hat{h}_j$, with operators \hat{h}_j as defined in Eq. (4), which reaches fidelities close to 1 with a remarkably small number $N_M \sim \mathcal{O}(10^4)$ of experimental runs. In our numerical experiments, we initialize each variational search with a random parameter vector \mathbf{g}^0 .

The blue curve in Fig. 3b) shows the behavior of the Uhlmann fidelity for a *classical protocol* to learn the EH as developed by [19] for system Hamiltonians, which we adapt here to EHs. This approach is based on measuring local observables $\hat{\mathcal{O}}_A$ which involve next- and next-next-nearest neighbor atomic currents (see Supplemental Material [42]). This is in contrast to QVL, where measurement of nearest-neighbour currents and local densities is sufficient. Fig. 3 shows results, where we estimate the scaling with a finite number of runs N_M by adding independent Gaussian noise to the observables \mathcal{O}_A , with zero mean, and variance $\epsilon^2 = \text{Var}(\mathcal{O}_A)/N_M$ (see Supplemental Material [42] for details). While QVL is bound to the restriction of implementing deformed Hamiltonians on the quantum device, convergence is achieved significantly earlier compared to CL. We note that for CL the number of experimental runs may be reduced by a factor $\sim N_A$ by grouping operators \mathcal{O}_A into commuting sets

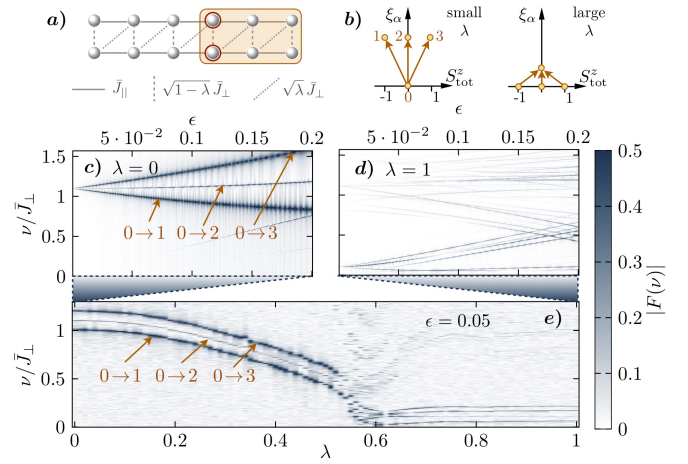


FIG. 4. *Entanglement spectroscopy of the Heisenberg model on a ladder*. a) Schematic of the setup, with subsystem A the right half of a 12-site ladder. We fix the ratio of horizontal to vertical couplings as $J_{\parallel}/J_{\perp} = 0.25$ and tune the relative strength of diagonal and vertical couplings with $\lambda \in [0, 1]$. b) Level scheme of the low-lying part of the entanglement spectra, indicating the dominant transitions illustrated here for $\epsilon = 0$. c) Measured entanglement spectrum (see main text), for small values ϵ of the perturbation, in the trivial phase ($\lambda = 0$). d) Same as c) at $\lambda = 1$. e) Measured entanglement spectra versus λ , at $\epsilon = 0.05\bar{J}_{\perp}$. All spectra are computed assuming 5000 measurements per observable at each time, measured up to $t = 1000/\bar{J}_{\perp}$.

which can be measured simultaneously.

On-device entanglement spectroscopy – The realization of the EH as a physical Hamiltonian on the quantum device allows measurement of the ES via spectroscopy [41] (see also [55]). Below we illustrate such a quantum post-processing step and simulate entanglement spectroscopy. To this end, we evolve the reduced system $\hat{\rho}_A$ once again, but now with a perturbation added to the EH, $\hat{H}_A^{\text{var}}(\mathbf{g}^{\text{opt}}) + \epsilon \hat{H}'$. For an appropriately chosen weak perturbation $\epsilon \hat{H}'$, the subsystem's response exhibits a quantum beat pattern with frequencies $\propto (\xi_{\alpha} - \xi_{\beta})$ that can be extracted by extrapolating $\epsilon \rightarrow 0$.

For simplicity, we consider the FHM on a ladder geometry [see Fig. 4a)] in the limit of large on-site interaction $U \gg J$, where it reduces to the Heisenberg model described by the Hamiltonian

$$\hat{H} = \sum_{\langle ij \rangle} \hat{h}_{ij}, \quad \hat{h}_{ij} = \bar{J} \sum_{a=x,y,z} \hat{\sigma}_i^a \hat{\sigma}_j^a, \quad (5)$$

with the sum running over neighboring sites on the ladder and we abbreviated $\bar{J} = J^2/(2U)$. We first apply our protocol to find an optimal EH, $\hat{H}_A^{\text{var}}(\mathbf{g}^{\text{opt}}) = \sum_{\langle ij \rangle_A} g_{ij}^{\text{opt}} \hat{h}_{ij}$, for the subsystem A indicated in Fig. 4a). The expected level structure of the corresponding ES is shown in Fig. 4b). In order to induce transitions that resolve the degeneracy of the low-lying levels, we then evolve with the learned EH perturbed by a local mag-

netic field, $\hat{H}' = \sum_{i_0=1,2} \vec{B}_{i_0} \cdot \hat{\sigma}_{i_0}$, supported on the two sites $i_0 = 1, 2$ at the edge of the entanglement cut indicated by the red circles in Fig. 4a), with $\vec{B}_1 = (1, 0, 1)$ and $\vec{B}_2 = (1, 0, -1/2)$.

We probe the response of the system by measuring $f(t) = \langle \sum_{j \in A} (-1)^{j_x + j_y} \hat{\sigma}_j^z(t) \rangle$ and plot the corresponding discrete cosine transformed spectrum $F(\nu)$ in Fig. 4c). The dominant lines correspond to transitions between the ground state and the first three excited states of \tilde{H}_A . Beating between excited states is significantly weaker due to the thermal occupation in the state $\hat{\rho}_A = \exp(-\tilde{H}_A)$. Our results clearly demonstrate that the values $\xi_{1,2,3} - \xi_0$ can be obtained by extrapolating the peak positions to $\epsilon = 0$. Importantly, the Zeeman-type splitting provides a clear resolution of the three-fold degeneracy. In an experiment, the ability to resolve this splitting will be limited by the coherence time of the device.

Measuring the ES and resolving its degeneracies constitutes a powerful tool to distinguish different quantum phases and identify topological order. Motivated by a recent experiment [56], we demonstrate this possibility in a generalized model, where we decrease the inter-leg couplings $\sqrt{1 - \lambda} \bar{J}_\perp$ while increasing new diagonal terms with strength $\lambda \bar{J}_\perp$, as indicated by the dashed and dotted links in Fig. 4a). This situation can be realized experimentally by displacing the two legs along the longitudinal direction, thereby smoothly interpolating between the previous analysis at $\lambda = 0$ and a Haldane phase at large λ . According to the Li-Haldane conjecture [57], this topological phase can be directly detected with the ES by counting the degeneracy of the ground state of \tilde{H}_A . The simulated spectrum in Fig. 4d) shows six dominant transition lines merging at $\nu \approx 0$ as $\epsilon \rightarrow 0$, which is a direct signature of the expected four-fold degeneracy of the ground state of \tilde{H}_A in the thermodynamic limit (in the zero magnetization sector). Finally, we sweep λ from 0 to 1, as illustrated in Fig. 4e), where the structure of resonant peaks shifts to $\nu = 0$. This directly reflects the expected changes of the ES [cf. Fig. 4b)], demonstrating that the on-device entanglement spectroscopy enables us to probe the transition from the trivial to the topological phase.

Outlook – Quantum variational learning provides a universal experimental toolset in the ongoing experimental effort to characterize novel equilibrium and non-equilibrium quantum phases [13] via their entanglement structure. Entanglement data obtained in the present framework can serve as input for further classical analysis, e.g., to train machine learning algorithms to identify quantum phases [58]. The fact that the optimization is performed *on device* is a key feature of our protocol, which not only enables the subsequent spectroscopy, but also provides robustness against potential miscalibration of the experimental setup. Additionally, since our cost

function is built from local observables, we expect the optimization to behave favorably under the barren plateau problem [59], though further investigations are required.

Acknowledgment – We thank L. K. Joshi, R. Kaubrügger, J. Carrasco, J. Yu, and B. Kraus for valuable discussions. We thank Ana Maria Rey and Murray Holland for a careful reading of the manuscript. We acknowledge funding from the European Union’s Horizon 2020 research and innovation programme under Grant Agreement No. 817482 (Pasquans) and No. 731473 (QuantERA via QT-FLAG). Furthermore, this work was supported by the Simons Collaboration on Ultra-Quantum Matter, which is a grant from the Simons Foundation (651440, P.Z.), and LASCEM by AFOSR No. 64896-PH-QC. M.D. is partly supported by the ERC under grant number 758329 (AGEnTh). A.E. acknowledges funding by the German National Academy of Sciences Leopoldina under the grant number LPDS 2021-02. BV acknowledges funding from the Austrian Science Foundation (FWF, P 32597 N), and the French National Research Agency (ANR-20-CE47-0005, JJC project QRand). The computational results presented here have been achieved (in part) using the LEO HPC infrastructure of the University of Innsbruck.

* These authors contributed equally.

- [1] *Manipulating Quantum Systems: An Assessment of Atomic, Molecular, and Optical Physics in the United States* (The National Academies Press, Washington, DC, 2020).
- [2] E. Altman, K. R. Brown, G. Carleo, L. D. Carr, E. Demler, C. Chin, B. DeMarco, S. E. Economou, M. A. Eriksson, K.-M. C. Fu, *et al.*, *PRX Quantum* **2**, 017003 (2021).
- [3] C. Gross and I. Bloch, *Science* **357**, 995 (2017).
- [4] H. Sun, B. Yang, H.-Y. Wang, Z.-Y. Zhou, G.-X. Su, H.-N. Dai, Z.-S. Yuan, and J.-W. Pan, (2009), [arXiv:2009.01426](https://arxiv.org/abs/2009.01426).
- [5] A. Mazurenko, C. S. Chiu, G. Ji, M. F. Parsons, M. Kanász-Nagy, R. Schmidt, F. Grusdt, E. Demler, D. Greif, and M. Greiner, *Nature* **545**, 462 (2017).
- [6] T. Hartke, B. Oreg, N. Jia, and M. Zwierlein, *Phys. Rev. Lett.* **125**, 113601 (2020).
- [7] J. Vijayan, P. Sompert, G. Salomon, J. Koepsell, S. Hirthe, A. Bohrdt, F. Grusdt, I. Bloch, and C. Gross, *Science* **367**, 186 (2020).
- [8] M. Holten, L. Bayha, K. Subramanian, C. Heintze, P. M. Preiss, and S. Jochim, *Phys. Rev. Lett.* **126**, 020401 (2021).
- [9] M. A. Nichols, L. W. Cheuk, M. Okan, T. R. Hartke, E. Mendez, T. Senthil, E. Khatami, H. Zhang, and M. W. Zwierlein, *Science* **363**, 383 (2019).
- [10] P. T. Brown, D. Mitra, E. Guardado-Sanchez, R. Nourafkan, A. Reymbaut, C.-D. Hébert, S. Bergeron, A.-M. S. Tremblay, J. Kokalj, D. A. Huse, P. Schauf, and W. S. Bakr, *Science* **363**, 379 (2019).
- [11] P. Scholl, M. Schuler, H. J. Williams, A. A. Eberharter, D. Barredo, K.-N. Schymik, V. Lienhard, L.-P. Henry,

- T. C. Lang, T. Lahaye, A. M. Läuchli, and A. Browaeys, (2020), [arXiv:2012.12268](#).
- [12] S. Ebadi, T. T. Wang, H. Levine, A. Keesling, G. Semeghini, A. Omran, D. Bluvstein, R. Samajdar, H. Pichler, W. W. Ho, S. Choi, S. Sachdev, M. Greiner, V. Vuletic, and M. D. Lukin, (2020), [arXiv:2012.12281](#).
- [13] G. Semeghini, H. Levine, A. Keesling, S. Ebadi, T. T. Wang, D. Bluvstein, R. Verresen, H. Pichler, M. Kalinowski, R. Samajdar, A. Omran, S. Sachdev, A. Vishwanath, M. Greiner, V. Vuletic, and M. D. Lukin, (2021), [arXiv:2104.04119](#).
- [14] C. Monroe, W. C. Campbell, L.-M. Duan, Z.-X. Gong, A. V. Gorshkov, P. W. Hess, R. Islam, K. Kim, N. M. Linke, G. Pagano, P. Richerme, C. Senko, and N. Y. Yao, *Rev. Mod. Phys.* **93**, 025001 (2021).
- [15] C. Kokail, C. Maier, R. van Bijnen, T. Brydges, M. K. Joshi, P. Jurcevic, C. A. Muschik, P. Silvi, R. Blatt, C. F. Roos, *et al.*, *Nature* **569**, 355 (2019).
- [16] C. Gross and W. S. Bakr, (2020), [arXiv:2010.15407](#).
- [17] A. Lukin, M. Rispoli, R. Schittko, M. E. Tai, A. M. Kaufman, S. Choi, V. Khemani, J. Léonard, and M. Greiner, *Science* **364**, 256 (2019).
- [18] M. Cerezo, A. Arrasmith, R. Babbush, S. C. Benjamin, S. Endo, K. Fujii, J. R. McClean, K. Mitarai, X. Yuan, L. Cincio, *et al.*, [arXiv preprint arXiv:2012.09265](#) (2020).
- [19] E. Bairey, I. Arad, and N. H. Lindner, *Phys. Rev. Lett.* **122**, 020504 (2019).
- [20] X.-L. Qi and D. Ranard, *Quantum* **3**, 159 (2019).
- [21] Z. Li, L. Zou, and T. H. Hsieh, *Phys. Rev. Lett.* **124**, 160502 (2020).
- [22] T. J. Evans, R. Harper, and S. T. Flammia, (2019), [arXiv:1912.07636](#).
- [23] C. Kokail, R. van Bijnen, A. Elben, B. Vermersch, and P. Zoller, *Nature Physics* **17**, 936 (2021).
- [24] K. Choo, C. W. Von Keyserlingk, N. Regnault, and T. Neupert, *Phys. Rev. Lett.* **121**, 086808 (2018).
- [25] A. Peruzzo, J. McClean, P. Shadbolt, M.-H. Yung, X.-Q. Zhou, P. J. Love, A. Aspuru-Guzik, and J. L. O’Brien, *Nature communications* **5**, 1 (2014).
- [26] R. LaRose, A. Tikku, É. O’Neel-Judy, L. Cincio, and P. J. Coles, *npj Quantum Information* **5**, 1 (2019).
- [27] S. Johri, D. S. Steiger, and M. Troyer, *Phys. Rev. B* **96**, 195136 (2017).
- [28] Y. Subaşı, L. Cincio, and P. J. Coles, *J. Phys. A Math. Theor.* **52**, 044001 (2019).
- [29] M. Cerezo, K. Sharma, A. Arrasmith, and P. J. Coles, [arXiv preprint arXiv:2004.01372](#) (2020).
- [30] S. Lloyd, M. Mohseni, and P. Rebentrost, *Nat. Phys.* **10**, 631 (2014).
- [31] C. Bravo-Prieto, D. García-Martín, and J. I. Latorre, *Phys. Rev. A* **101**, 062310 (2020).
- [32] N. Regnault, (2015), [arXiv:1510.07670](#).
- [33] R. Haag, *Local quantum physics: Fields, particles, algebras* (Springer Science & Business Media, 2012).
- [34] H. Casini, M. Huerta, and R. C. Myers, *JHEP* **1105**, 036 (2011).
- [35] J. J. Bisognano and E. H. Wichmann, *J. Math. Phys.* **16**, 985 (1975).
- [36] For a generalization within CFT to finite subsystems of radius R , see Ref. [34, 46?] who proved that the deformation takes a parabolic shape, $\beta(\mathbf{x}) = 2\pi(R^2 - \mathbf{x}^2)/(2R)$, or similarly with the chord length.
- [37] M. Pourjafarabadi, H. Najafzadeh, M.-S. Vaezi, and A. Vaezi, *Phys. Rev. Res.* **3**, 013217 (2021).
- [38] V. Eisler, G. Di Giulio, E. Tonni, and I. Peschel, **2020**, 103102 (2020).
- [39] G. Giudici, T. Mendes-Santos, P. Calabrese, and M. Dalmonte, *Phys. Rev. B* **98**, 134403 (2018).
- [40] F. Parisen Toldin and F. F. Assaad, *Phys. Rev. Lett.* **121**, 200602 (2018).
- [41] M. Dalmonte, B. Vermersch, and P. Zoller, *Nat. Phys.* **14**, 827 (2018).
- [42] C. Kokail, B. Sundar, T. Zache, A. Elben, B. Vermersch, M. Dalmonte, R. van Bijnen, and P. Zoller, “Supplementary information: Quantum variational learning of the entanglement hamiltonian,”.
- [43] G. Vidal, *Phys. Rev. Lett.* **91**, 147902 (2003).
- [44] X. Turkeshi, T. Mendes-Santos, G. Giudici, and M. Dalmonte, *Phys. Rev. Lett.* **122**, 150606 (2019).
- [45] W. Zhu, Z. Huang, and Y.-C. He, *Phys. Rev. B* **99**, 235109 (2019).
- [46] J. Cardy and E. Tonni, *Journal of Statistical Mechanics: Theory and Experiment* **2016**, 123103 (2016).
- [47] J. Carrasco, A. Elben, C. Kokail, B. Kraus, and P. Zoller, *PRX Quantum* **2**, 010102 (2021).
- [48] X. Qiu, J. Zou, X. Qi, and X. Li, *npj Quantum Information* **6**, 1 (2020).
- [49] N. Goldman, J. C. Budich, and P. Zoller, *Nat. Phys.* **12**, 639 (2016).
- [50] We note that here the variational search is constrained to $g_j > 0$ for all j . In the case that $g_j < 0$ are allowed, a solution with $g_j = -g_{j+1}$ does exist which freezes the particles on the individual lattice sites. To exclude this solution, additional observables like nearest-neighbour tunneling amplitudes are required.
- [51] C. Schweizer, M. Lohse, R. Citro, and I. Bloch, *Phys. Rev. Lett.* **117**, 170405 (2016).
- [52] S. Kébler and F. Marquardt, *Phys. Rev. A* **89**, 061601 (2014).
- [53] A. M. Läuchli and J. Schliemann, *Phys. Rev. B* **85**, 054403 (2012).
- [54] To be precise, we consider a family of reconstructed states $\hat{\rho}_A^{\text{var}}(\mathbf{g}, \beta) = Z_A^{-1}(\beta) e^{-\beta \hat{H}_A^{\text{var}}(\mathbf{g})}$ with $Z_A(\beta) = \text{Tr} \left[e^{-\beta \hat{H}_A^{\text{var}}(\mathbf{g})} \right]$, and define the fidelity as $\mathcal{F}(\hat{\rho}_A^{\text{var}}(\mathbf{g}), \hat{\rho}_A) = \max_{\beta} \left[\text{Tr} \left(\sqrt{\sqrt{\hat{\rho}_A} \hat{\rho}_A^{\text{var}}(\mathbf{g}, \beta) \sqrt{\hat{\rho}_A}} \right) \right]^2$.
- [55] H. Pichler, G. Zhu, A. Seif, P. Zoller, and M. Hafezi, *Phys. Rev. X* **6**, 041033 (2016).
- [56] P. Sompet, S. Hirthe, D. Bourgund, T. Chalopin, J. Bibo, J. Koepsell, P. Bojović, R. Verresen, F. Pollmann, G. Salomon, *et al.*, (2021), [arXiv:2103.10421](#).
- [57] H. Li and F. D. M. Haldane, *Phys. Rev. Lett.* **101**, 010504 (2008).
- [58] E. P. Van Nieuwenburg, Y.-H. Liu, and S. D. Huber, *Nat. Phys.* **13**, 435 (2017).
- [59] M. Cerezo, A. Sone, T. Volkoff, L. Cincio, and P. J. Coles, *Nature Communications* **12**, 1791 (2021).